

Article

Morphologies of Comb-like Polyacrylic Acid/Polyacrylate Copolymers as Functions of the Degree of Derivatization with $n\text{-C}_{22}\text{H}_{45}$ Side Chains

Tomoya Okada ¹, Mizuho Ishii ¹, Harumi Sato ² and Go Matsuba ^{1,*} 

¹ Graduate School of Organic Materials Engineering, Yamagata University, 4-3-16 Jonan, Yonezawa 992-8510, Yamagata, Japan

² Graduate School of Human Development and Environment, Kobe University, Kobe 657-8501, Hyogo, Japan; hsato@tiger.kobe-u.ac.jp

* Correspondence: gmatsuba@yz.yamagata-u.ac.jp

Abstract: Polymers with crystallizable side chains have numerous applications, and their properties depend on their crystal morphologies and phase separation. Structural analysis on a wide spatial scale plays an important role in controlling the thermal properties and higher-order structures of these polymers. In this study, we elucidated the melting and crystallization processes of copolymers with varying crystallizable side-chain fractions over a wide spatial range. Differential scanning calorimetry revealed that the enthalpies of melting and crystallization increased linearly with increasing crystallizable side-chain fraction. The results of wide-angle X-ray scattering indicated that the crystal lattice was hexagonal. Conversely, spherulite-like higher-order architectures with linear structures and radial spreading were observed in the highly crystallizable components, but no micrometer-scale structures were observed in the less crystallizable components. In situ small-angle X-ray scattering was used to elucidate the phase separation and mixing processes. Lamellar crystallites were observed at crystallizable side-chain fractions of >55 wt.%, whereas small crystallites were observed at fractions of <45 wt.%. At temperatures above the order-disorder transition temperature, density fluctuations caused by correlation holes were observed. These properties have a strong effect on the crystallizable side-chain fraction.

Keywords: grafted copolymer; crystal morphology; structural analysis



Citation: Okada, T.; Ishii, M.; Sato, H.; Matsuba, G. Morphologies of Comb-like Polyacrylic Acid/Polyacrylate Copolymers as Functions of the Degree of Derivatization with $n\text{-C}_{22}\text{H}_{45}$ Side Chains. *Polymers* **2023**, *15*, 4663. <https://doi.org/10.3390/polym15244663>

Academic Editors: Asterios (Stergios) Pispas, Vasile Cojocaru, Gabriela Mărginean and Doina Frunzăverde

Received: 18 October 2023

Revised: 3 December 2023

Accepted: 6 December 2023

Published: 11 December 2023



Copyright: © 2023 by the authors. Licensee MDPI, Basel, Switzerland. This article is an open access article distributed under the terms and conditions of the Creative Commons Attribution (CC BY) license (<https://creativecommons.org/licenses/by/4.0/>).

1. Introduction

Comb-like polymers, which comprise polymer main chains and pendant side chains, exhibit characteristic crystalline structures, self-assembly morphologies, and melt properties [1–4]. Accordingly, their crystallization and segmental packing differ from those of typical linear polymers because of the influences of their structural compositions and side-chain lengths [5–10]. Consequently, the manipulation of comb-like polymers, which exhibit different behaviors in terms of side-chain crystallization, is useful in understanding their local chain-packing modes [6,11–15]. In addition, the polymer backbone, side-chain length, and chemical linkages significantly influence the characteristic chain packing and side-chain crystallization of a comb-like polymer. When longer side chains are introduced along the polymer backbone, an ordered packing structure is typically formed because of the increased number of crystallizable CH_2 units [16,17].

The attachment of appropriate side chains to their polymeric backbones may result in materials with remarkable structures and advanced functionalities, such as charge transport, in addition to optical properties and responsive performance [12,18]. Understanding the aggregated structures of comb-like polymers is advantageous in designing responsive materials with novel architectures. Furthermore, the pendant side chains do not fully participate in crystallization, and only the C atoms that are positioned away from the main

chain enter the crystalline phase [4,16]. Thus, the minimum requirement or critical number of crystallizable C atoms varies with the stiffness of the polymer backbone [19,20]. In addition, the lengths of the side alkyl groups determine the crystal domains of the comb-like polymers, which exhibit distinct structural and packing patterns. Previous research regarding *n*-alkylated poly(*p*-benzamide) [21], polyethyleneimine [22], chitosan [23], and polyvinyl alcohol [24] comb-like polymers with side-chain lengths ranging from 12 to 22 carbon atoms showed that the melting temperatures (T_m) and enthalpies (ΔH_m) of the paraffin-like crystallites depend strongly on the sizes of the alkyl domains.

The comb-like polymer used in this study exhibits the same chemical structure as Intellimer™, which is an acrylic adhesive [25,26]. Intellimer™ is under development for use as a thermosensitive adhesive based on the significant changes in its various properties with temperature. It is also under consideration for use as a film whose transparency and opacity may be controlled with temperature. Its physical properties have been summarized in several studies [26,27]. In this study, we used a semi-crystalline graft copolymer of short- and long-chain esters of polyacrylic acid, with polyacrylic acid as the main-chain backbone. The long-chain ester, which behaves as a side chain, contains the linear alkyl group $C_nH_{(2n+1)}$, which crystallizes at low temperatures. Heating to the melting point of the linear alkyl moiety causes a transition from a semi-crystalline to an amorphous state. This transition may modulate properties such as the thermosensitive viscosity, permeability, and adhesion.

Therefore, by manipulating the primary structures of the crystallizable side chains, it is possible to vary the temperature at which the phase transition between crystallization and melting occurs, i.e., to change the adhesion and release properties. Additionally, the melting point and viscoelastic properties may be altered by varying the side-chain density. Such adhesives find numerous applications in the field of electronics, including in lithography [28] and the fabrication of indium gallium zinc oxide panels [29–31]. In addition, as their viscoelasticities vary with temperature, they are used in microcapsule coatings for seeds, with an emphasis on sustainability [32,33], and in films to control permeability to air [34]. Additionally, graft polymerization of materials such as Intellimer™ onto the surfaces of microparticles to generate temperature-dependent microparticles has been studied [35]. The relationship between the crystal structure of a comb polymer and its adhesive properties has been elucidated via detailed analysis of the crystal structure, of changes in the higher-order crystal structure with temperature, and of the adhesion and release properties of the material [36]. In this study, thermal measurements and spatially extended structural analyses were used to evaluate the crystallization and melting processes of comb polymers with different weight percents of crystallizable side-chain components. The fraction dependences of the crystalline components are the focus of this study. In situ wide-angle X-ray scattering (WAXS) and synchrotron radiation were used to evaluate crystal growth and melting, and we evaluated their sub-micrometer structures using in situ small-angle X-ray scattering (SAXS). Depolarized light scattering and polarized light and atomic force microscopy (AFM) were used to study the micrometer-scale structure of the material. Accordingly, the degree of crystallinity, crystal size, density fluctuation, and higher-order structure as functions of temperature were elucidated and summarized.

2. Materials and Methods

2.1. Materials

Figure 1 shows a simplified chemical structure of the graft copolymer consisting of acrylic acid, methyl acrylate, and monomers randomly grafted with acrylic acid-linked alkyl side chains. The main chains, which consist of polyacrylic acid, poly(methyl acrylate), and 1-docosanol ($C_{22}H_{45}OH$)-linked polyacrylic acid, were supplied by Nitta, Osaka, Japan. *n*-Alkyl $C_{22}H_{45}$, as shown in Figure 1, crystallizes. The graft copolymer Intellimer™ is a trademark of Landec (Menlo Park, CA, USA), which has a commercial licensing partnership with Nitta. The ratio of acrylic acid monomers to side-chain $C_{22}H_{45}/CH_3/H$ was controlled

by mass. Table 1 shows the proportions of 1-docosanol acrylate, methyl acrylate, and acrylic acid employed. The weight-averaged molecular weight for all samples is about 500,000.

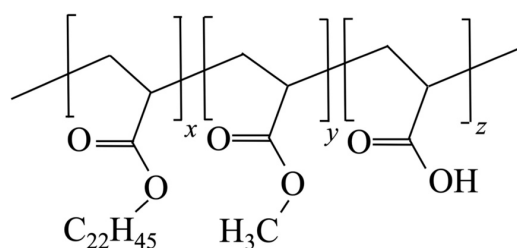


Figure 1. Simplified chemical structure of the random polyacrylic acid-type copolymer with *n*-C₂₂H₄₅ crystallizable side-chain components.

Table 1. Ratios (wt.%) of the monomers with side chains of C₂₂H₄₅/CH₃/H and ratio of the crystallizable side chain (mol%).

Sample	Monomer (wt.%) with Side-Chain C ₂₂ H ₄₅ /CH ₃ /H	Crystallizable Side Chain (mol%)
0 wt.%	0/95/5	0
20 wt.%	20/75/5	5.3
30 wt.%	30/65/5	8.7
45 wt.%	45/50/5	15
55 wt.%	55/40/5	21
70 wt.%	70/25/5	34
90 wt.%	90/5/5	65
100 wt.%	100/0/0	100

2.2. Measurements

Differential scanning calorimetry (DSC) was performed using a DSC Q200 (TA Instruments, New Castle, DE, USA), which was calibrated using the T_m values of In and cyclohexane standards. Samples of ~5 mg were heated in Al pans from 0 to 100 °C at a rate of 10 °C/min. The melting or crystallization temperature (T_m or T_x) is the onset temperature of endothermy or exothermy.

SAXS and WAXS were performed using the BL-6A beamline (Photon Factory, High Energy Accelerator Research Organization, Tsukuba, Japan) at a wavelength of 0.15 nm [37,38]. The respective camera lengths used in SAXS and WAXS were 931 and 243 mm, and the respective detectors used in SAXS and WAXS were PILATUS 1M and PILATUS 100K (DECTRIS, Baden, Switzerland). The ranges of the scattering vector q ($=4\pi\sin\theta/\lambda$, 2θ : scattering angle, λ : wavelengths used in SAXS and WAXS) were from 6.0×10^{-2} to 2.5 and 8 to 19 nm⁻¹, and the thickness of each sample was approximately 200 μm. During in situ SAXS and WAXS, the sample film was sandwiched between two polyether ether ketone films and mounted on a Linkam 10002L hot stage (Linkam Scientific Instruments, Redhill, UK) for temperature control. FIT2D software (version 12.077, European Synchrotron Radiation Facility, Grenoble, France) was used for data processing, including contrast control of the 2D patterns and the creation of 1D profiles of the obtained 2D patterns.

AFM was performed to observe the internal structure on the sub-micrometer scale using an Agilent 5500 (Agilent Technologies, Santa Clara, CA, USA). The tapping mode was used to measure the topography, and the phase contrast was measured. The probes used were PPP-NCL probes (NANOSENSORS, Neuchatel, Switzerland) with respective spring constants and resonance frequencies of ~50 N/m and ~190 kHz, yielding a respective scan size and image resolution of 20 × 20 nm and 256 × 256. After the samples were bonded to Si substrates, Kapton films were applied to their surfaces.

Depolarized small-angle light scattering using a PP-1000 system (Otsuka Electronics, Osaka, Japan) was performed to observe the micrometer-scale higher-order structures. The camera length was 50 mm, and the light source was a He-Ne laser ($\lambda = 654$ nm). The range of the scattering vector q was $0.30\text{--}2.0\ \mu\text{m}^{-1}$, and the sample, with a thickness of $\sim 40\ \mu\text{m}$, was sandwiched between two cover glasses. The temperature was controlled using the Linkam 10002 L hot stage [39]. Optical microscopy was performed using a VW-5000 microscope (Keyence, Osaka, Japan) equipped with high-speed charge-coupled device (CCD) camera attachments [40].

Raman spectra were measured in the $400\text{--}100\ \text{cm}^{-1}$ range using a LabRAM HR Evolution (HORIBA, Kyoto, Japan) equipped with a Sincerity CCD detector at an excitation wavelength of 532 nm. The respective spectral resolution, laser power, exposure time, and number of scans used in Raman spectroscopy were $0.5\ \text{cm}^{-1}$, 100 mW, 15 s, and 5. Temperature-dependent Raman spectroscopy was performed using a T95-HS temperature controller (Linkam Scientific Instruments) [41].

3. Results and Discussion

3.1. Thermodynamic Phenomena

Figure 2a shows the DSC thermograms obtained at cooling and heating rates of $10\ ^\circ\text{C}/\text{min}$. In the thermogram of the 0 wt.% sample, T_m and the crystallization temperature T_x are not observed; thus, no crystallization occurs in this sample. In contrast, T_x and T_m increase as the fraction of crystallizable side-chain components increases above 20 wt.%. Figure 2b shows that the glass transition temperature of the 0 wt.% sample is approximately $24.2\ ^\circ\text{C}$. Figure S1 and Table S1 shows DSC thermograms of 55 wt.% for the definition of T_m and T_x and the peak temperature and finishing temperature for melting and crystallization. The correlations between the content of the crystallizable side-chain component and T_m and T_x are shown in Figure 2c. Even at 45 wt.%, the T_m exceeds that of 1-docosane ($\text{C}_{22}\text{H}_{46}$) crystals ($43.9\ ^\circ\text{C}$) [42]. The higher melting point may be due to the attachment of the crystallizable side chains to the main chain, which hinders molecular motion. The enthalpy (ΔH) and the crystallization enthalpy increase as the weight percent of the crystallizable side-chain component increases [43].

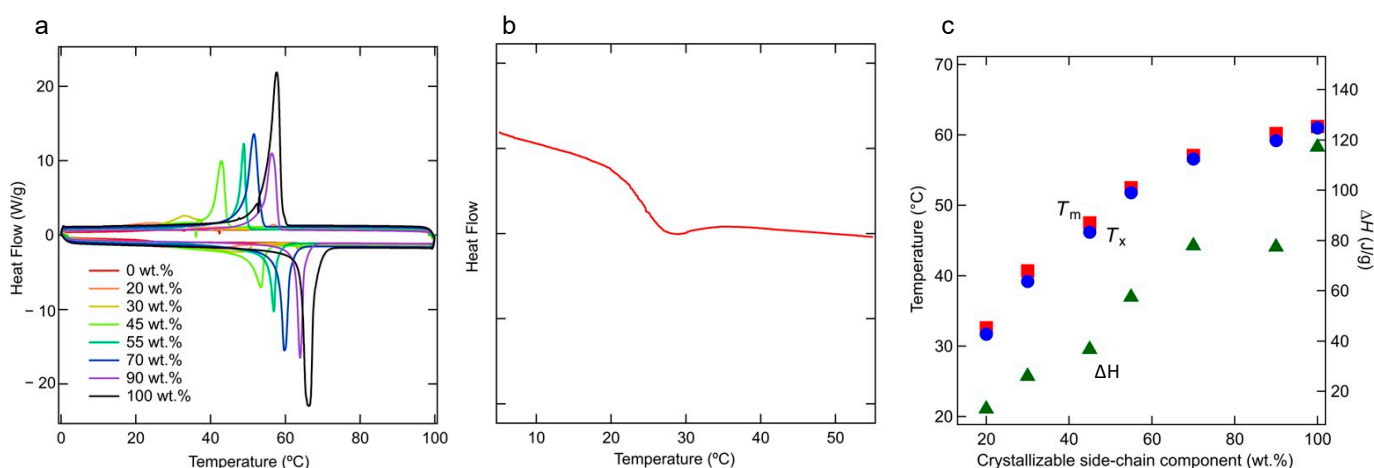


Figure 2. Effects of fraction on the thermal properties. The DSC thermograms reveal crystallization during cooling from the molten state and melting due to heating of the crystalline/amorphous material between 0 and $100\ ^\circ\text{C}$ (heating and cooling rates = $10\ ^\circ\text{C}/\text{min}$) (a). Magnified DSC thermogram of the 0 wt.% sample (b). Melting (T_m ; solid squares) and crystallization temperatures (T_x ; solid circles) and melting enthalpies (solid triangles) at different fractions (c).

3.2. High-Ordered Structures at the Submicron and Micron Scales

Figure 3a,b shows the depolarized small-angle light-scattering profiles and polarized optical micrographs of the 45 and 70 wt.% samples at $25\ ^\circ\text{C}$. Below 45 wt.%, a very

low scattering intensity was observed, indicating that the microscale structure forms slowly, whereas at 70 wt.%, a peak was observed at about $q_p = 0.7 \mu\text{m}^{-1}$. Figure 3c shows $10 \mu\text{m}$ -scaled spherulite-like structures under 70 wt. % conditions, as observed via AFM with linear structures. From the depolarized small-angle scattering pattern, an average spherulite size, R_s , was calculated from the peak position, q_p , using Equation (1) [44,45].

$$R_s = \frac{4.09}{q_p}, \quad (1)$$

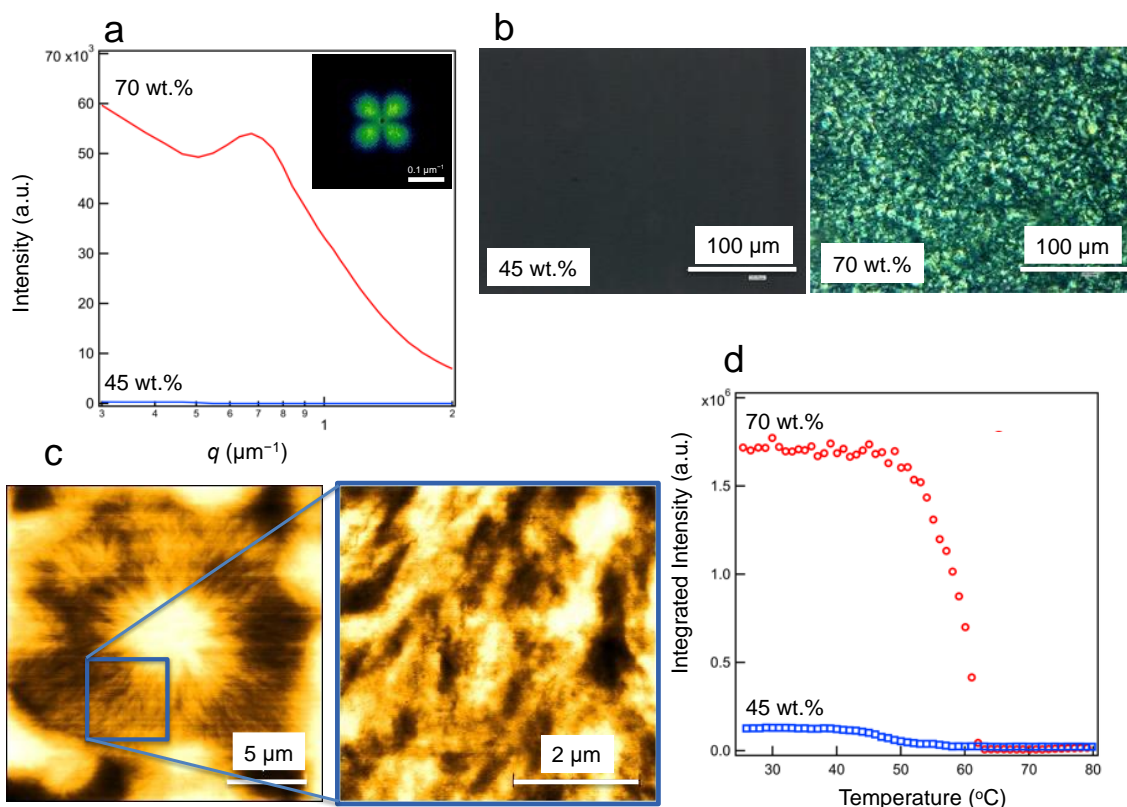


Figure 3. Micrometer-scale structures of the samples at different fractions. (a) Depolarized light-scattering profiles of the 70 and 45 wt.% samples and 2D scattering profiles of 70 wt.% sample. (b) Polarized optical micrographs of the 70 and 45 wt.% samples. (c) AFM images of the 70 wt.% sample at different magnifications, showing the spherulite-like structure and a magnified view of the linear structure. (d) Temperature dependence of the integrated scattering intensity of the depolarized light.

Here, q_p is the magnitude of the scattering vector at the peak position in the four-leaf clover patterns in the inset of Figure 3a. Therefore, the R_s was $5.8 \mu\text{m}$. Figure 3d shows the temperature dependence of the total integrated scattering intensity during heating. Scattering is no longer observed upon melting. The temperature at which scattering completely disappears coincides with the melting point measured using DSC, indicating that these higher-order architectures display crystalline-derived oriented structures.

3.3. Crystal Lattice Determined via WAXS

Figure 4a–c shows the results of WAXS of copolymers with different side-chain fractions following heating of their crystalline states. In the profiles of all samples, we observed that the diffraction peak at $q = 15.3 \text{ nm}^{-1}$ starts to decrease above T_m because the crystals are melting. Therefore, these peaks were considered with respect to the crystal structure of the crystallizable side-chain component.

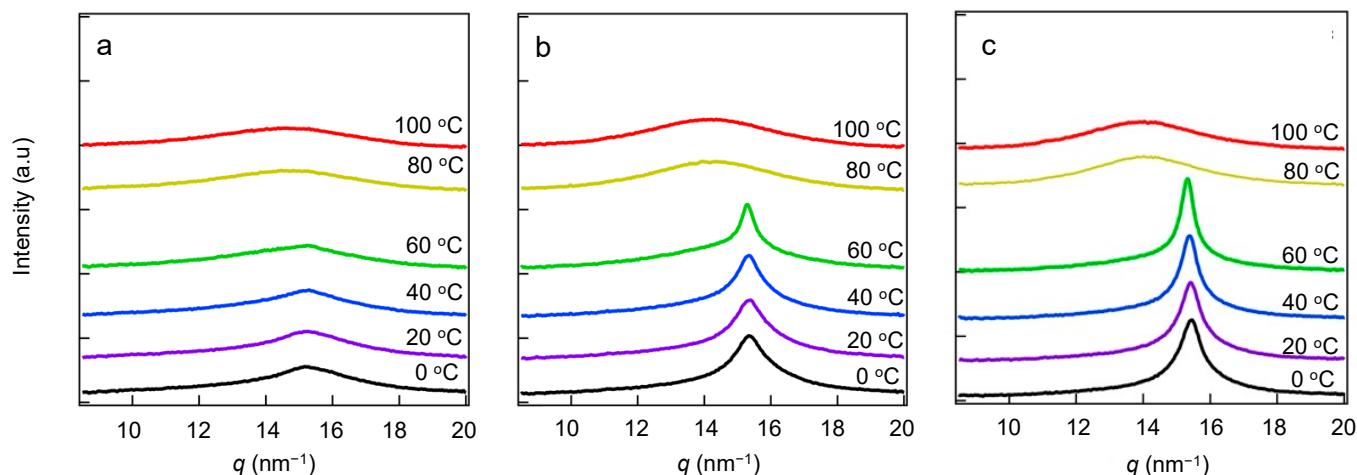


Figure 4. Temperature dependences of the in situ WAXS profiles of the 30 (a), 55 (b), and 70 wt.% (c) samples at a heating rate of 10 °C/min during heating of their crystalline/amorphous states from 0 °C. The baseline of each profile is shifted up or down to avoid overlap.

Figure S2 shows the results of WAXS of the copolymers at 0 °C. We could find no crystalline peak for the crystallizable side-chain component of 0 wt.%, with only an amorphous halo observed; thus, the main chain may not crystallize above 0 °C. If the alkyl portion of the side chain exhibits the same orthorhombic structure as the polyethylene crystal, crystal-diffraction peaks should be present, in addition to the amorphous halo. However, only one amorphous halo and one diffraction peak were observed in this study. For a detailed analysis, we calculated the correlation length d based on the peak position using Equation (2).

$$d = \frac{2\pi}{q_{\text{peak}}}, \quad (2)$$

where q_{peak} is the peak position in the scattering profile. Spacing values d_{WAXS} of 0.42 nm were observed in the hexagonal structures of the alkyl chains [11,46,47]. During heating, the diffraction peak representing the hexagonal crystalline structure decreases and shifts based on the smaller angle, and only an amorphous halo at $q \approx 14.0 \text{ nm}^{-1}$ is observed when the material is melted. We compared the crystallinities at different temperatures. The ratio of the crystalline regions in the WAXS profiles, $R_c(T)$, is defined in Equation (3).

$$R_c(T) = \frac{I_{\text{cry}}(T)}{I_{\text{cry}}(T) + I_{\text{amo}}(T)}, \quad (3)$$

where $I_{\text{cry}}(T)$ and $I_{\text{amo}}(T)$ are the respective areas of the crystalline and amorphous portions of the WAXS profiles. Figure S3 shows the decomposition of the 70 wt.% sample at 0 °C based on the WAXS profile. $R_c(T)$ depends on the crystallinity, and we evaluated the crystalline size, L_{hkl} , using the Scherrer equation (Equation (4)).

$$L_{hkl} = \frac{k\lambda}{\beta \cos \theta} \quad (4)$$

Figure 5a shows the $R_c(T)$ and L_{110} of the side-chain crystalline component at 0 °C, which is below the melting point. $R_c(T)$ increases with increasing fraction. In particular, in the case of 70 and 90 wt.%, $R_c(T)$ increases slightly. These results are consistent with the results for ΔH from DSC thermograms in Figure 2c. Similarly, L_{110} increases with increasing fraction.

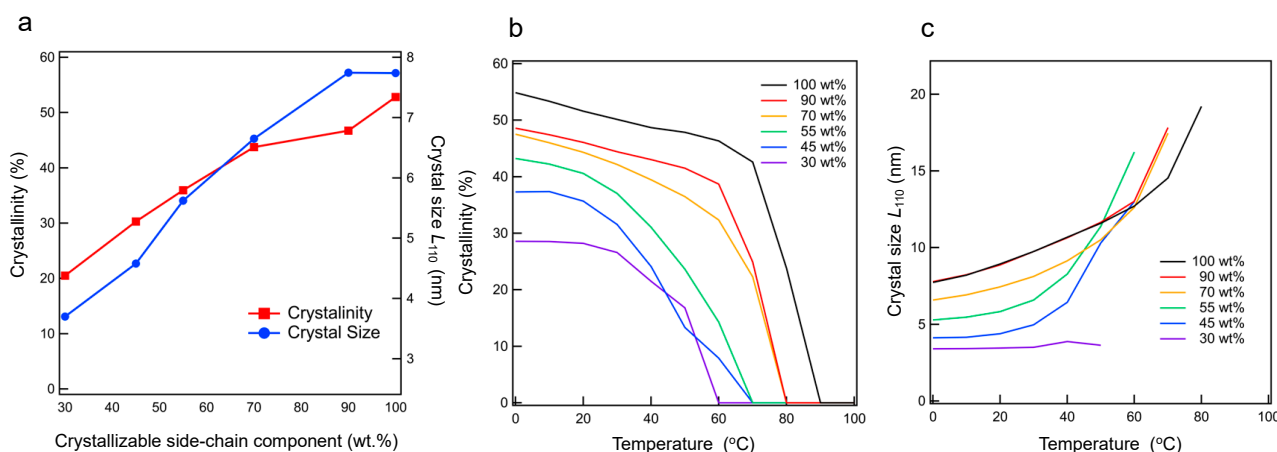


Figure 5. (a) Ratio $R_c(T)$ of Equation (2) and crystal size L_{110} of the Scherrer equation (Equation (3)), as determined based on the in situ WAXS profiles of the samples with different side-chain fractions at 0 °C. (b) $R_c(T)$ and (c) L_{110} at different temperatures during heating of the crystalline/amorphous states of the samples from 0 °C.

Figure 5b,c shows the respective temperature dependences of $R_c(T)$ and L_{110} during heating. $R_c(T)$ decreases with increasing temperature, becoming zero above the melting point determined via DSC. At fractions above 45 wt.%, L_{hkl} increases with increasing temperature, while $R_c(T)$ decreases with temperature. These results suggest that the increase in L_{110} is due to the aggregation and enlargement of small crystals with partially melting side-chain crystals. However, at a low fraction (30 wt. %), L_{110} is independent of temperature, even at temperatures close to the T_m . Linear long-chain organic molecules are known to form lamellar intermediate phases (also called rotator phases) between their fully ordered crystalline phases and their isotropic liquid phases. The review by Cholakova and Denkov suggested that endothermic or exothermic peaks were observed during phase transition of the rotator phase of *n*-alkane [48]. Even in graft copolymers, endothermic peaks were observed [49]. We discuss the rotator phase between T_m and T_{m_finish} . From the report by Cholakova and Denkov [50], the difference between the melting point and the transition temperature of the rotator phase of $C_{22}H_{46}$ is 1.4 °C. On the other hand, the difference between T_m and T_{m_finish} is between 10.4 and 16.3 °C in Table S1. These data suggest that both the transition from fully crystalline to rotator phase and the transition from the rotator phase to isotropic melt occur over a wide temperature range in the case of comb-like copolymers, making it difficult to distinguish between these two transition processes. Consequently, one endothermic peak was observed in Figure 2a.

3.4. Sub-Micrometer-Scale Structure Determined via In Situ SAXS

Figure 6a,b shows the SAXS profiles obtained at 0 and 100 °C, respectively. As shown in Figure 6a, the peak at $q \approx 1.5 \text{ nm}^{-1}$ shifts to a higher q as the fraction of the crystalline alkyl side chain increases, and the profile of the 0 wt.% sample displays very weak peaks. Therefore, the peak represents the ratio of the polyacrylic acid main chains to crystalline alkyl side chains.

Meanwhile, as shown in Figure 6b, broad peaks were observed at $q \approx 1.5 \text{ nm}^{-1}$ and the secondary peaks are no longer observed. The correlation length d is calculated based on the peak position q_{peak} of the SAXS profile using Equation (1), and Table 2 shows the correlation lengths d at 0 and 100 °C. Above 30 wt.%, the correlation length at 100 °C is smaller than that at 0 °C. The correlation length decreases with an increase in the content of the crystallizable side-chain component. Based on the DSC thermograms, the crystallinity increases as the content of the crystallizable side-chain component increases. The correlations calculated from SAXS measurements are those between crystals and crystallites or between crystalline and amorphous components. A low crystallizable side-chain component weight percent is associated with a low correlation length between crystals. In other words, the increase in

the correlation length with a decreasing crystalline component weight percent is due to the increase in the amorphous component, which increases the thickness of the amorphous region between crystals and thus the distance between crystals.

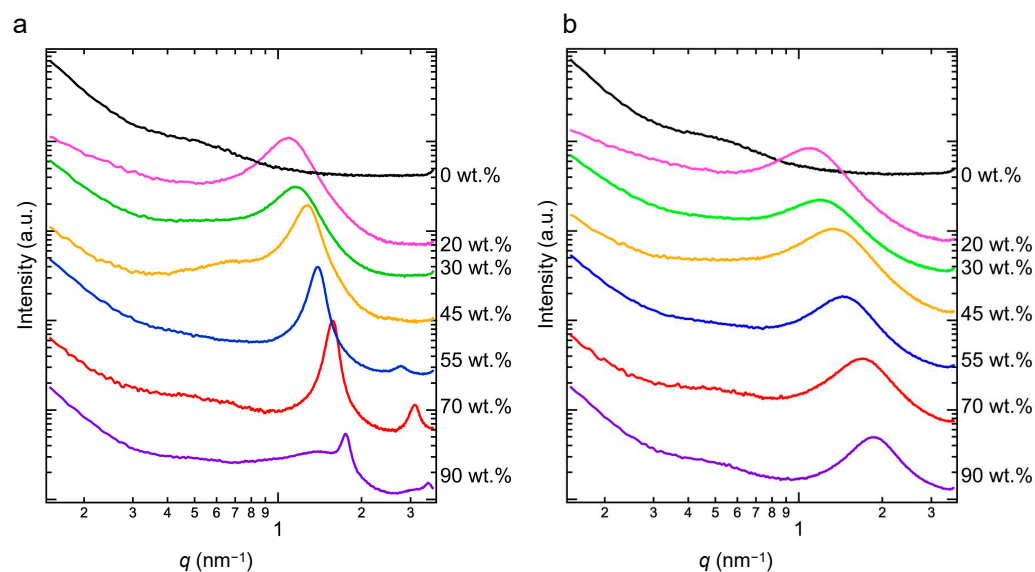


Figure 6. In situ SAXS profiles obtained at 0 (a) and 100 °C (b). The baseline of each profile is shifted up or down to avoid overlap.

Table 2. Correlation lengths of the samples with different weight percents of the crystallizable side-chain component annealed at 0 and 100 °C.

Sample	Correlation Length at 0 °C [nm]	Correlation Length at 100 °C [nm]
20 wt.%	5.92 ± 0.05	6.16 ± 0.07
30 wt.%	5.58 ± 0.07	5.44 ± 0.08
45 wt.%	5.08 ± 0.01	4.83 ± 0.08
55 wt.%	4.62 ± 0.02	4.34 ± 0.07
70 wt.%	4.09 ± 0.02	3.85 ± 0.07
90 wt.%	3.59 ± 0.02	3.33 ± 0.07

Figure 7a–c shows the temperature dependences of the SAXS profiles of the samples with crystalline alkane side-chain fractions of 30 (a), 55 (b), and 70 wt.% (c) during heating from 0 to 100 °C. There is a sharp peak at $q = 1.5$ nm⁻¹ due to the crystalline phase. As shown in Figure 7b,c, a secondary peak is observed close to $q = 3.0$ nm⁻¹ at temperatures below that at which the crystals are completely melted, T_{m_finish} in Table S1. Figure 6a shows the same secondary peaks in the profiles of the 45, 55, 70, and 90 wt.% samples. These results suggest that these copolymers contain lamellar microdomains with sizes of 3.59–4.62 nm. The correlation length is 1.3–1.6-fold longer than the fully extended crystallizable side-chain length of 2.8 nm. Thus, the SAXS profiles indicate that the polymer's main chains form a lamellar plane with the *n*-docosane side chains. We evaluated the crystal thickness of the 100 wt.% sample using SAXS and DSC, and Figure S4 shows the Raman spectra obtained during heating. The longitudinal acoustic vibrations of the molecular alkyl chains were observed using low-frequency Raman spectroscopy.

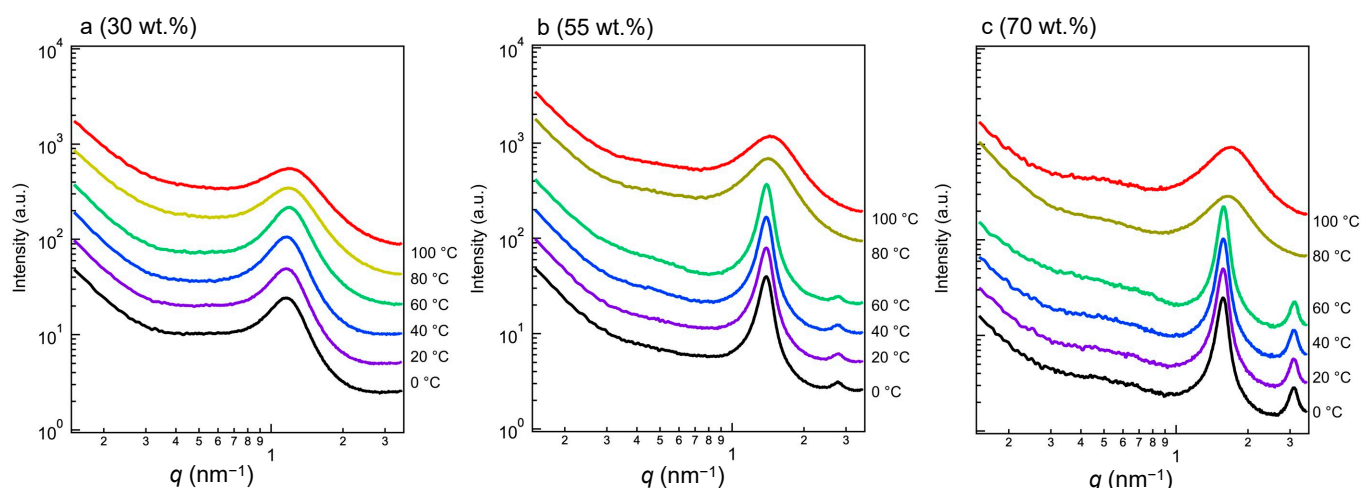


Figure 7. Temperature dependences of the in situ SAXS profiles of the samples with contents of the crystallizable side-chain component of 30 (a), 55 (b), and 70 wt.% (c) at a heating rate of 10 °C/min during heating from their crystalline/amorphous states from 0 °C. The baseline of each profile is shifted up or down to avoid overlap.

Above T_{m_finish} or at a low crystalline alkane side-chain weight percent, only the broader peak is observed, with no secondary peak, i.e., when the secondary peak is absent, as shown in Figure 7a, the observation of one SAXS peak may be insufficient to support the conclusion that a lamellar morphology has formed within the polymer complex [51–58]. Therefore, we observe small crystallites, even below T_m . At the T_m of the onset temperature of melting, the peaks of SAXS profiles of the samples becomes weak. At the temperatures at which the melting process finishes (T_{m_finish} ; in Table S1), only single broad peaks are seen due to the disordered states of the polymers. Thus, the complexes may exhibit characteristic copolymer-like fraction fluctuations (correlation hole effects) [53–55]. For a more detailed analysis, we focused on the order-disorder transition (ODT) and the melting process at about T_m . The change in the scattering pattern across the ODT enables the determination of the ODT temperature (T_{ODT}). There are several methods based on mean-field theory of identifying T_{ODT} using the results of SAXS. Two of the most common methods used are plots of (i) the reciprocal of the maximum scattering intensity ($I_m^{-1}(q_m)$) against the reciprocal of the absolute temperature (T^{-1}) and (ii) the correlation length d_{SAXS} ($=2\pi/q_m$) against T^{-1} . According to Leibler's mean-field theory, $I_m^{-1}(q_m)$ should decrease linearly with T^{-1} in the disordered state:

$$I_m^{-1}(q_m) \sim a - \frac{b}{T}, \quad (5)$$

where a and b are positive constants [56–58]. Equation (5) assumes the temperature dependence of the Flory-Huggins segmental interaction parameter between the polyacrylic acid main chain and crystallizable alkane side chains. Leibler's theory predicts that d_{SAXS} or q_m in the disordered state is essentially independent of the temperature if we omit the small temperature variation due to the temperature dependences of the radii of gyration of the copolymer chains $R_g(T)$.

$$d_{SAXS}/R_g(T) \sim T^0. \quad (6)$$

Thus, in the context of mean-field theory, the deviations in the temperature dependences of $I_m^{-1}(q_m)$ in Equation (5) and d_{SAXS} in Equation (6) are attributed to the onset of the disordering process upon heating, and they may thus be used to determine T_{ODT} . Figure 8a–c show plots of $I_m^{-1}(q_m)$ and d for the different crystallized copolymer components as functions of T^{-1} . As shown in Figure 8a–c, $I_m^{-1}(q_m)$ and d_{SAXS} are constant with respect to T^{-1} at temperatures $< T_m$ because the crystals in small crystallites (Figure 8a) and the lamellar structure (Figure 8b,c) prevent an increase in density fluctuations during

heating. The gray region in Figure 8 shows the temperature during melting process from DSC measurements in Figure 2a. A linear decrease in $I_m^{-1} (q_m)$ is observed at temperatures above the crystal melting temperature, which is a result consistent with the theoretical predictions of Equation (5). Based on Equation (6), d is independent of T (or T^{-1}) but increases slightly with T^{-1} , and Sakurai and Nandan also observed a slight increase in d [51,54]. This increase occurs because the copolymer may exhibit an upper critical solution temperature-type phase separation, and the components of the main chain and crystallizable side chains should be mixed at the molecular level at temperatures $> T_m$. At temperatures just above T_m , $I_m^{-1} (q_m)$ exhibits a peak, and d decreases abruptly when the temperature increases, as shown in Figure 8b,c. This behavior is similar to the temperature dependences of star polymers [59]. The respective T_{ODT} values of the 55 and 70 wt.% samples are approximately 69 and 80 °C. Conversely, based on Figure 8a, T_{ODT} is 56 °C, which exceeds the T_m values of the crystallites in the 30 wt.% sample.

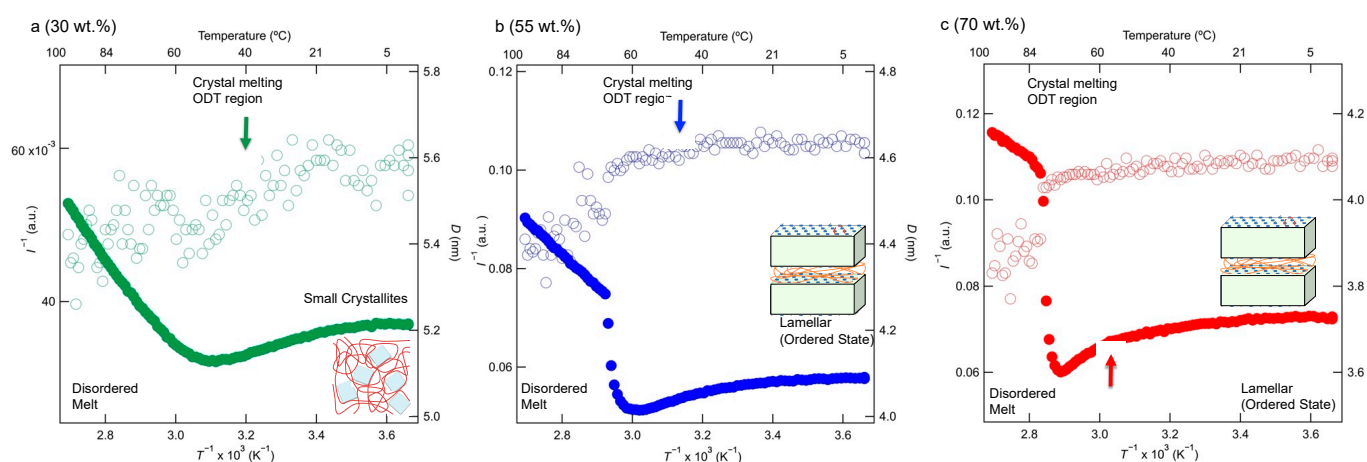


Figure 8. Dependences on the reciprocal of the absolute temperature of the reciprocals of the peak intensities $I_m^{-1} (q_m)$ (filled circles) and correlation lengths d (open circles) of the samples with weight percents of the crystallizable side-chain component of 30 (a), 55 (b), and 70 wt.% (c) at a heating rate of 10 °C/min during heating of their crystalline/amorphous states from 0 °C. The arrows indicate the melting points based on the DSC thermograms.

3.5. Modeling the Large-Scale Structures of the Grafted Copolymers with Crystallizable Side-Chain Components

Based on these results, models of the crystallizable side-chain copolymers were developed. First, when the weight percent of the crystallizable side-chain component is low (below 30 wt.%), very few crystals were observed, and the morphology depends on the main chain, which is almost randomly coiled. Therefore, small crystallites with low crystallinities were observed. As the crystallizable side-chain weight percent increases, the crystallinities and widths of the crystals also increase. WAXS revealed crystals with hexagonal structures, with correlation values of 0.42 nm. SAXS revealed lamellar structures with sizes of several nanometers in the more crystallizable components, as the correlation length of the lamellar structure is sufficiently smaller than that of the C22 extended chain. Conversely, small crystallites were observed within the less crystallizable components. Above T_{m_finish} , the crystallites are completely molten and an ODT occurs. Figure 9 shows a schematic summary of the structure of the copolymer. However, when crystallizable side-chain components were present below 20 wt.%, we could not analyze the small-crystallites and phase separation because of very small crystallinity. When the weight percent of the crystallizable side-chain components is above 90 wt.%, the sample amount is very small, making it difficult to analyze the phase separation and crystal morphology for in-situ SAXS/WAXS measurements.

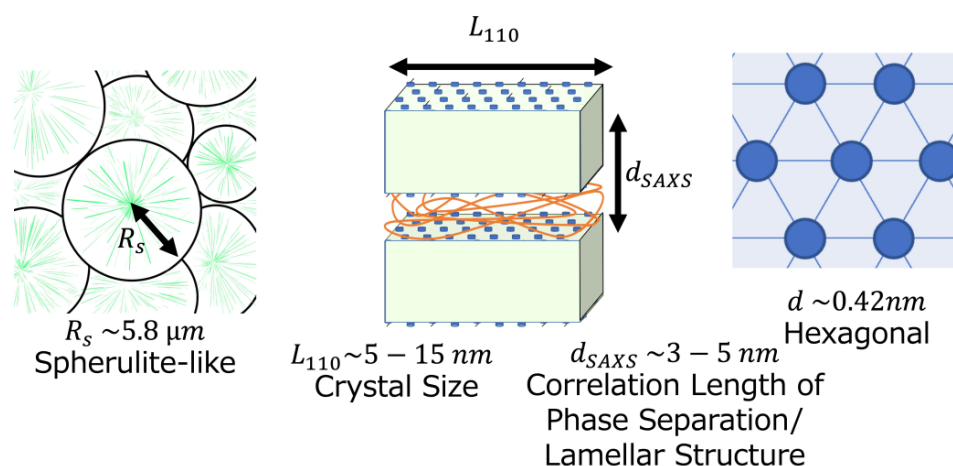


Figure 9. Schematic of the hierarchical structure of the copolymer with side chains with highly crystallizable components and a high weight percent of the crystallizable side-chain component (such as 70 wt.%). The arrows are the sizes of spherulites, R_s , crystal L_{110} , and correlation of phase separation and lamellar structure, d_{SAXS} .

4. Conclusions

In situ observations were used to elucidate the melting and crystallization processes of alkyl side-chain polymers with crystallizable side-chain fractions over a broad range of spatial scales. As the weight percent of the crystallizable side-chain component increased, T_m and T_x increased. The ΔH values of the crystals were also evaluated. In addition, the results of WAXS revealed that the crystal lattice was hexagonal, and SAXS revealed a several-nm-scale lamellar structure with highly crystalline components, as the correlation length of the lamellar structure was sufficiently smaller than that of the C22 extended chain, based partially on Raman spectroscopy below T_m . Between T_m and T_{m_finish} , it is difficult to distinguish the processes of transition from crystalline to the rotator phase and melting by DSC. Above T_m , the crystallites were molten. Further, above T_{m_finish} , an ODT occurred. At a larger scale, a spherulite-like higher-order architecture with a linear structure and radial spreading was observed.

Supplementary Materials: The following supporting information can be downloaded at: <https://www.mdpi.com/article/10.3390/polym15244663/s1>, Figure S1: T_m and T_x definition from DSC thermograms of 55 wt.% sample; Figure S2: WAXS profiles of different crystallizable side-chain components at 0 °C; Figure S3: The peak decomposition of WAXS profiles of 70 wt.% at 0 °C; Figure S4: Analysis of the temperature dependence of the Raman spectrum of the 100 wt.% sample; Table S1: List of T_m and T_x , the peak temperature and the finishing temperature during melting and crystallization processes. References [60,61] are cited in the supplementary materials.

Author Contributions: Formal analysis, T.O. and M.I.; Investigation, T.O. and M.I.; Visualization, T.O.; Writing—original draft, T.O.; Methodology, M.I. and H.S.; Resources, H.S.; Supervision, G.M.; Writing—review and editing, G.M.; Funding Acquisition, G.M. All authors have read and agreed to the published version of the manuscript.

Funding: This study was funded by Japan Society for the Promotion of Science KAKENHI grants (grant nos. JP19H05721 and JP21H01994).

Institutional Review Board Statement: Not applicable.

Data Availability Statement: Raw data were generated at Yamagata University. Derived data supporting the findings of this study are available from the corresponding author, G.M., on request.

Acknowledgments: SAXS was performed with the approval of the Photon Factory Program Advisory Committee (proposal nos. 2019G521, 2021G524, and 2022G027), and synchrotron radiation studies were performed at the BL43IR beamlines of SPring-8 (Sayo, Japan) with the approval of the Japan Synchrotron Radiation Research Institute (proposal nos. 2020A1046, 2020A1427, 2020A1262,

2021A1628, 2021A1195, and 2021A1196). This study was partially conducted via Joint Research Program Nos. R2009, R3005, and R40015 of the Molecular Photoscience Research Center of Kobe University (Kobe, Japan). We are grateful to Shogo Isoda, Takumi Kato, and Minoru Nanchi (Nitta) for research collaboration and sample provision. The authors thank Yuji Fujiyama, Tomoko Shimeki, Yusaku Suzuki, Kazuki Suzuki, and Kaito Yui (Yamagata University, Yamagata, Japan) for their early and related works.

Conflicts of Interest: The authors declare no conflict of interest.

References

1. Shi, H.; Zhao, Y.; Dong, X.; Zhou, Y.; Wang, D. Frustrated crystallisation and hierarchical self-assembly behaviour of comb-like polymers. *Chem. Soc. Rev.* **2013**, *42*, 2075–2099. [[CrossRef](#)] [[PubMed](#)]
2. Kim, K.; Kang, D.A.; Park, J.T.; Kim, K.C.; Kim, J.H. Synthesis, structure and gas separation properties of ethanol-soluble, amphiphilic POM-PBHP comb copolymers. *Polymer* **2019**, *180*, 121700. [[CrossRef](#)]
3. Liang, H.; Wang, Z.; Sheiko, S.S.; Dobrynin, A.V. Comb and bottlebrush graft copolymers in a melt. *Macromolecules* **2019**, *52*, 3942–3950. [[CrossRef](#)]
4. Mao, H.; Wang, H.; Li, J.; Zhang, L.; Shi, J.; Shi, H. Side-chain crystallization and segment packing of poly(isobutylene-*alt*-maleic anhydride)-*g*-alkyl alcohol comb-like polymers. *Polymer* **2020**, *202*, 122721. [[CrossRef](#)]
5. Andrikopoulos, K.; Vlassopoulos, D.; Voyiatzis, G.A.; Yiannopoulos, Y.D.; Kamitsos, E.I. Molecular orientation of hairy-rod polyesters: Effects of side chain length. *Macromolecules* **1998**, *31*, 5465–5473. [[CrossRef](#)]
6. Babur, T.; Gupta, G.; Beiner, M. About different packing states of alkyl groups in comb-like polymers with rigid backbones. *Soft Matter* **2016**, *12*, 8093–8097. [[CrossRef](#)] [[PubMed](#)]
7. Danke, V.; Gupta, G.; Huth, H.; Schawe, J.E.K.; Beiner, M. Polymorphic states and phase transitions in a comb-like polymer having a rigid polyester backbone and flexible side chains. *Thermochim. Acta* **2019**, *677*, 162–168. [[CrossRef](#)]
8. Hirabayashi, T.; Kikuta, T.; Kasabou, K.; Yokota, K. Main-chain flexibility and sidechain crystallization of widely spaced comb-like polymers. *Polym. J.* **1998**, *20*, 693–698. [[CrossRef](#)]
9. Meng, J.; Tang, X.; Zhang, Z.; Zhang, X.; Shi, H. Fabrication and Properties of poly(polyethylene glycol octadecyl ether methacrylate). *Thermochim. Acta* **2013**, *574*, 116–120. [[CrossRef](#)]
10. Imai, S.; Arakawa, M.; Nakanishi, Y.; Takenaka, M.; Aoki, H.; Ouchi, M.; Terashima, T. Water-assisted microphase separation of cationic random copolymers into sub-5 nm lamellar materials and thin films. *Macromolecules* **2022**, *55*, 9113–9125. [[CrossRef](#)]
11. Greenberg, S.A.; Alfrey, T. Side Chain Crystallization of *n*-alkyl polymethacrylates and polyacrylates¹. *J. Am. Chem. Soc.* **1954**, *76*, 6280–6285. [[CrossRef](#)]
12. Shi, H.; Wang, H.; Yin, Y.; Liu, G.; Zhang, X.; Wang, D. Chain packing and phase transition of N-hexacosylated polyethyleneimine comb-like polymer: A combined investigation by synchrotron X-ray scattering and FTIR spectroscopy. *Polymer* **2013**, *54*, 6261–6266. [[CrossRef](#)]
13. Gopi, S.; Kontopoulou, M.; Ramsay, B.A.; Ramsay, J.A. Manipulating the structure of medium-chain-length polyhydroxyalkanoate (MCL-PHA) to enhance thermal properties and crystallization kinetics. *Int. J. Biol. Macromol.* **2018**, *119*, 1248–1255. [[CrossRef](#)] [[PubMed](#)]
14. Barnard, E.; Pfkwa, R.; Maiz, J.; Müller, A.J.; Klumperman, B. Synthesis, structure, and crystallization behavior of amphiphilic heteroarm molecular brushes with crystallizable poly(ethylene oxide) and *n*-alkyl side chains. *Macromolecules* **2020**, *53*, 1585–1595. [[CrossRef](#)]
15. Ebata, K.; Hashimoto, Y.; Yamamoto, S.; Mitsuishi, M.; Nagano, S.; Matsui, J. Nanophase separation of poly(*N*-alkyl acrylamides): The dependence of the formation of lamellar structures on their alkyl side chains. *Macromolecules* **2019**, *52*, 9773–9780. [[CrossRef](#)]
16. Shi, H.; Zhao, Y.; Jiang, S.; Xin, J.H.; Rottstegge, J.; Xu, D.; Wang, D. Order-disorder transition in Eicosylated polyethyleneimine comblike polymers. *Polymer* **2007**, *48*, 2762–2767. [[CrossRef](#)]
17. Xu, H.; Gao, Y.; Li, J.; Wang, H.; Shi, H. Thermal performance and phase transformation of S-alkylated poly(vinyl chloride) comb-like polymers. *Polymer* **2018**, *153*, 362–368. [[CrossRef](#)]
18. Tekin, E.; Egbe, D.A.M.; Kranenburg, J.M.; Ulbricht, C.; Rathgeber, S.; Birckner, E.; Rehmann, N.; Meerholz, K.; Schubert, U.S. Effect of side chain length variation on the optical properties of PPE-PPV hybrid polymers. *Chem. Mater.* **2008**, *20*, 2727–2735. [[CrossRef](#)]
19. Zheng, W.; Levon, K.; Laakso, J.; Oesterholm, J.E. Characterization and solid-state properties of processable *N*-alkylated polyanilines in the neutral state. *Macromolecules* **1994**, *27*, 7754–7768. [[CrossRef](#)]
20. Lee, J.L.; Pearce, E.M.; Kwei, T.K. Side-chain crystallization in alkyl-substituted semiflexible polymers. *Macromolecules* **1997**, *30*, 6877–6883. [[CrossRef](#)]
21. Shi, H.F.; Zhao, Y.; Zhang, X.Q.; Zhou, Y.; Xu, Y.H.; Zhou, S.R.; Wang, D.J.; Han, C.C.; Xu, D.F. Packing mode and conformational transition of alkyl side chains in *N*-alkylated poly(*p*-benzamide) comb-like polymer. *Polymer* **2004**, *45*, 6299–6307. [[CrossRef](#)]
22. Shi, H.F.; Zhao, Y.; Zhang, X.Q.; Jiang, S.C.; Wang, D.J.; Han, C.C.; Xu, D.F. Phase transition and conformational variation of *N*-alkylated branched poly(ethyleneimine) comblike polymer. *Macromolecules* **2004**, *37*, 9933–9940. [[CrossRef](#)]

23. Zhou, Y.; Shi, H.F.; Zhao, Y.; Men, Y.F.; Jiang, S.C.; Rottstegge, J.; Wang, D.J. Confined crystallization and phase transition in semi-rigid chitosan containing long chain alkyl groups. *CrystEngComm* **2011**, *13*, 561–567. [[CrossRef](#)]
24. Li, L.J.; Shi, H.F.; Zhang, X.X. Preparation and characterization of Octadecylated poly(vinyl alcohol) polymers. *Adv. Mater. Res.* **2012**, *482–484*, 1921–1924. [[CrossRef](#)]
25. Greene, L.; Phan, L.X.; Schmitt, E.E.; Mohr, J.M. Side-chain crystallizable polymers for temperature-activated controlled release. In *Polymeric Delivery Systems*; American Chemical Society: Washington, DC, USA, 1993; pp. 244–256. [[CrossRef](#)]
26. Okada, M.; Nakano, S.; Yamashita, K.; Kawahara, S.; Matsui, S. Direct patterning on side chain crystalline polymer by thermal nanoimprinting using mold without antisticking layer. *Microelectron. Eng.* **2011**, *88*, 2084–2087. [[CrossRef](#)]
27. Shimizu, H. Adhesive bonding technologies in production engineering. Recent trend on intelligent material. *J. Jpn Soc. Precis. Engi* **1998**, *64*, 210–213. [[CrossRef](#)]
28. Sun, H. Recent progress in low temperature nanoimprint lithography. *Microsyst. Technol.* **2015**, *21*, 1–7. [[CrossRef](#)]
29. Yang, S.; Bak, J.Y.; Yoon, S.M.; Ryu, M.K.; Oh, H.; Hwang, C.S.; Kim, G.H.; Park, S.K.; Jang, J. Low-temperature processed flexible in-Ga-Zn-O thin-film transistors exhibiting high electrical performance. *IEEE Electron Dev. Lett.* **2011**, *32*, 1692–1694. [[CrossRef](#)]
30. Min, S.Y.; Cho, W.J. Resistive switching characteristic improvement in a single-walled carbon nanotube random network embedded hydrogen silsesquioxane thin films for flexible memristors. *Int. J. Mol. Sci.* **2021**, *22*, 3390. [[CrossRef](#)]
31. Min, J.G.; Cho, W.J. Chitosan-based flexible memristors with embedded carbon nanotubes for neuromorphic electronics. *Micromachines* **2021**, *12*, 1259. [[CrossRef](#)]
32. Greene, L.C.; Meyers, P.A.; Springer, J.T.; Banks, P.A. Biological evaluation of pesticides released from temperature-responsive microcapsules. *J. Agric. Food Chem.* **1992**, *40*, 2274–2278. [[CrossRef](#)]
33. Johnson, G.A.; Hicks, D.H.; Stewart, R.F.; Duan, X. Use of temperature-responsive polymer seed coating to control seed germination. *Acta Hort.* **1999**, *504*, 229–236. [[CrossRef](#)]
34. Kim, D.; Seo, J. A review: Breathable films for packaging applications. *Trends Food Sci. Technol.* **2018**, *76*, 15–27. [[CrossRef](#)]
35. Parrinello, C.A.; Bounds, C.O.; Liveri, M.L.T.; Pojman, J.A. Thermal frontal polymerization with a thermally released redox catalyst. *J. Polym. Sci. A Polym. Chem.* **2012**, *50*, 2337–2343. [[CrossRef](#)]
36. Matsuba, G.; Fujiyama, Y.; Shimeki, T.; Ishii, M.; Nanchi, M.; Kato, T.; Kawahara, S. The effect of tackifier on temperature-sensitive adhesives with polymers of crystallizable side-chain. *J. Soc. Mater. Sci. Jpn* **2019**, *68*, 20–25. [[CrossRef](#)]
37. Igarashi, N.; Watanabe, Y.; Shinohara, Y.; Inoko, Y.; Matsuba, G.; Okuda, H.; Mori, T.; Ito, K. Upgrade of the small angle X-ray scattering beamlines at the photon factory. *J. Phys. Conf. S.* **2011**, *272*, 012026. [[CrossRef](#)]
38. Takagi, H.; Igarashi, N.; Mori, T.; Saijo, S.; Ohta, H.; Nagatani, Y.; Kosuge, T.; Shimizu, N. Upgrade of small angle X-ray scattering beamline BL-6A at the photon factory. *AIP Conf. Proc.* **2016**, *1741*, 030018. [[CrossRef](#)]
39. Nishida, K.; Ogawa, H.; Matsuba, G.; Konishi, T.; Kanaya, T. A high-resolution small-angle light scattering instrument for soft matter studies. *J. Appl. Crystallogr.* **2008**, *41*, 723–728. [[CrossRef](#)]
40. Zhao, Y.; Hayasaka, K.; Matsuba, G.; Ito, H. In situ observations of flow-induced precursors during shear flow. *Macromolecules* **2013**, *46*, 172–178. [[CrossRef](#)]
41. Miwa, Y.; Nagahama, T.; Sato, H.; Tani, A.; Takeya, K. Intermolecular interaction of tetrabutylammonium and tetrabutylphosphonium salt hydrates by low-frequency Raman observation. *Molecules* **2022**, *27*, 4743. [[CrossRef](#)]
42. Domańska, U.; Łachwa, J.; Morawski, P.; Malanowski, S.K. Phase equilibria and volumetric properties in binary mixtures containing branched chain ethers (methyl 1,1-dimethylethyl ether or ethyl 1,1-dimethylethyl ether or methyl 1,1-dimethylpropyl ether or ethyl 1,1-dimethylpropyl ether). *J. Chem. Eng. Data* **1999**, *44*, 974–984. [[CrossRef](#)]
43. Chickos, J.S.; Hanshaw, W. Vapor pressures and vaporization enthalpies of the *n*-alkanes from C₂₁ to C₃₀ at *T* = 298.15 K by correlation gas chromatography. *J. Chem. Eng. Data* **2004**, *49*, 77–85. [[CrossRef](#)]
44. Stein, R.S.; Rhodes, M.B. Photographic light scattering by polyethylene films. *J. Appl. Phys.* **1960**, *31*, 1873–1874. [[CrossRef](#)]
45. Stein, R.S.; Wilson, P.R. Scattering of light by polymer films possessing correlated orientation fluctuations. *J. Appl. Phys.* **1962**, *33*, 1914–1922. [[CrossRef](#)]
46. Inomata, K.; Sakamaki, Y.; Nose, T.; Sasaki, S. Solid-state structure of comb-like polymers having *n*-octadecyl side chains I. Cocrystallization of side chain with *n*-octadecanoic acid. *Polym. J.* **1996**, *28*, 986–991. [[CrossRef](#)]
47. Mondieig, D.; Rajabalee, F.; Metivaud, V.; Oonk, H.A.J.; Cuevas-Diarte, M.A. *n*-alkane binary molecular alloys. *Chem. Mater.* **2004**, *16*, 786–798. [[CrossRef](#)]
48. Cholakova, D.; Denkov, N. Rotator phases in alkane systems: In bulk, surface layers and micro/nano-confinements. *Adv. Colloid Interface Sci.* **2019**, *269*, 7–42. [[CrossRef](#)]
49. Danke, V.; Beiner, M.; Saalwächter, K.; Schäfer, M. Structure and dynamics in a polymorphic nanophase-separated stiff comblike polymer. *Macromolecules* **2019**, *52*, 6943–6952. [[CrossRef](#)]
50. Cholakova, D.; Tsvetkova, K.; Tcholakova, S.; Denkov, N. Rheological properties of rotator and crystalline phases of alkanes. *Colloids Surf. A Physicochem. Eng. Asp.* **2022**, *634*, 127926. [[CrossRef](#)]
51. Nandan, B.; Lee, C.; Chen, H.; Chen, W. Molecular architecture effect on the microphase separations in supramolecular comb-coil complexes of polystyrene—Block—Poly(2-vinylpyridine) with dodecylbenzenesulfonic acid: (AB)_nA_n block-arm star copolymer. *Macromolecules* **2005**, *38*, 10117–10126. [[CrossRef](#)]
52. Huh, J.; Ikkala, O.; ten Brinke, G. Correlation hole effect in comblike copolymer systems obtained by hydrogen bonding between homopolymers and end-functionalized oligomers. *Macromolecules* **1997**, *30*, 1828–1835. [[CrossRef](#)]

53. Chen, H.-L.; Hsiao, M.-S. Self-assembled mesomorphic complexes of branched poly(ethylenimine) and Dodecylbenzenesulfonic acid. *Macromolecules* **1999**, *32*, 2967–2973. [[CrossRef](#)]
54. Sakurai, S.; Mori, K.; Okawara, A.; Kimishima, K.; Hashimoto, T. Evaluation of segmental interaction by small-angle x-ray scattering based on the random-phase approximation for asymmetric, polydisperse triblock copolymers. *Macromolecules* **1992**, *25*, 2679–2691. [[CrossRef](#)]
55. Russell, T.P.; Hjelm, R.P., Jr.; Seeger, P.A. Temperature dependence of the interaction parameter of polystyrene and poly(methyl methacrylate). *Macromolecules* **1990**, *23*, 890–893. [[CrossRef](#)]
56. Leibler, L. Theory of microphase separation in block copolymers. *Macromolecules* **1980**, *13*, 1602–1617. [[CrossRef](#)]
57. Leibler, L.; Benoit, H. Theory of correlations in partly labelled homopolymer melts. *Polymer* **1981**, *22*, 195–201. [[CrossRef](#)]
58. Staropoli, M.; Raba, A.; Hövelmann, C.H.; Krutyeva, M.; Allgaier, J.; Appavou, M.-S.; Keiderling, U.; Stadler, F.J.; Pyckhout-Hintzen, W.; Wischniewski, A.; et al. Hydrogen bonding in a reversible comb polymer architecture: A microscopic and macroscopic investigation. *Macromolecules* **2016**, *49*, 5692–5703. [[CrossRef](#)]
59. Floudas, G.; Hadjichristidis, N.; Iatrou, H.; Pakula, T.; Fischer, E.W. Microphase separation in model 3-miktoarmstar copolymers (simple graft and terpolymers). 1. Statics and kinetics. *Macromolecules* **1994**, *27*, 7735–7746. [[CrossRef](#)]
60. Claudy, P.; Letoffe, J.M. Phase transitions in even n-alkanes C_nH_{2n+2} , $n = 16–28$. Characterization by differential calorimetric analysis and by thermo-optical analysis. Effect of deuteration. *Calorim. Anal. Therm.* **1991**, *22*, 281.
61. Schaufele, R.F. Chain Shortening in Polymethylene Liquids. *J. Chem. Phys.* **1968**, *49*, 4168. [[CrossRef](#)]

Disclaimer/Publisher’s Note: The statements, opinions and data contained in all publications are solely those of the individual author(s) and contributor(s) and not of MDPI and/or the editor(s). MDPI and/or the editor(s) disclaim responsibility for any injury to people or property resulting from any ideas, methods, instructions or products referred to in the content.